Flow Distribution in the Fiber Lumen Side of a Hollow-Fiber Module

Little attention has been paid to the flow distribution among many thousands of fibers in the hollow-fiber modules of artificial kidney, ultrafiltration, and reverse osmosis devices despite its potential importance in the efficiency of the module. Numerical study by a finite-difference method, as well as experiment by direct sampling from individual fibers and high-speed photography of a color tracer, has shown that there exists a significant degree of nonuniformity in the flow distribution, which depends on the manifold design, the Reynolds number, and the pressure drop along the fibers.

Joong Kon Park, Ho Nam Chang
Department of Chemical Engineering
Korea Advanced Institute of
Science and Technology
Seoul, Korea

SCOPE

Hollow-fiber membrane modules are favored for use in diffusion and ultrafiltration devices owing to their high surface area-to-volume ratio as compared to flat or spiral-wound modules. The greatest applications are seen in artificial kidneys, ultrafiltration for protein purification, and reverse osmosis. Since Rony (1971) proposed using this kind of device as an enzyme reactor, many enzymes have been immobilized. Recently Inloes et al. (1983) have immobilized *E. coli* to produce β-lactamase. Babcock et al. (1980) used hollow-fiber membrane in extracting uranium.

In spite of popular applications in separation and reaction/separation fields, little attention has been paid to the design and the efficiency of hollow-fiber devices. Engasser et al. (1980) showed in their residence time distribution study that there was a dead region in the fiber lumen of the hollow-fiber enzyme reactor at a low flow rate, and the size of the dead region became smaller with the increase of flow rates. Agish et al. (1975) showed experimentally that the blood distributed preferentially through the fibers located in the periphery of the module and that the distribution became worse at higher flow rates. In these two examples experimental results are in conflict with each other; it is difficult to understand the reason for this unless the problem is approached systematically.

The typical device consists of inlet tube, upstream manifold, hollow-fiber bundles, downstream manifold, and outlet tube. Since all components of the device potentially affect flow distribution, numerical studies with a finite-difference method have been performed for the effects of manifold design (cylindrical and conical), Reynolds numbers ranging from 50 to 200, and pressure drop in the fibers on the flow distribution. And a few important results are to be verified experimentally using the methods of direct sampling from individual fibers, high-speed photography of a color tracer, and residence time distribution study.

CONCLUSIONS AND SIGNIFICANCE

Calculations of the flow distributions among many thousands of hollow fibers have been made possible with the use of a modified finite-difference scheme combining the characteristics of wall jet and manifold flow. Numerical simulation shows that the approaching velocity profile of the flow at the inlet of the manifold becomes closer to that of the Poiseuille flow as the height of the inlet manifold increases. With the cylindrical manifold the highest velocity occurs in the fiber located at the center and the lowest occurs in the

Correspondence concerning this paper should be adressed to Ho Nam Chang.
Joong Kon Park is currently at the Dept. of Chemical Engineering, Kyungpook National University, Taegu, Korea.

fibers located near the center. With the conical manifold the trend is the same at and near the center. But the peripheral velocity decreases significantly below the average and the local maximum velocity occurs between the local minimum point near the center and the periphery. These characteristics become more significant with the smaller pressure drop parameter in the fiber designated by K, the lower manifold height, and the higher Reynolds number (RE). Thus relatively uniform distribution may be obtained when K is large, RE is small, and the manifold height is high. For the cylindrical manifold the attachment of a rear manifold tends to smooth nonuniform flow distributions, compared to those with one manifold at the inlet.

In general, the experimental results are in good agreement with the theoretical results. The velocity through a fiber at the center is highest in most cases, and the minimum near the center was detected. The effect of RE is well supported experimentally. In the bundle with a cylindrical manifold the velocity near the edge is nearly the average velocity, but that with a conical manifold is below the average, as predicted. The residence time distribution study for the bundle with the upstream and downstream manifolds and the visual observation show qualitatively that the fluid in the fibers in the center region passes the bundle faster than the fluid in other regions. Also, at a low RE the distributions become more uniform. The high-speed photographs of a dye tracer confirm that the fluid in the center moves faster than the rest in the bundle with cylindrical and conical manifolds. Also, the transit times measured at the center and the peripheral region are in good agreement with the predicted times.

The results of this study will be directly applicable to the design of artificial kidneys, which should eliminate a dead region, and will help in designing better performing hollow-fiber devices. It would be interesting to reassess the performance of heat exchangers using a similar approach.

Introduction

Figure 1 shows a typical hollow-fiber membrane module consisting of inlet manifold, fiber bundle with many thousands of fibers, and outlet manifold. In the inlet manifold the fluid entering from the inlet tube impinges upon the bundle surface perpendicularly to form a pseudostagnation point flow in the center, and flows radially toward the periphery, discharging some portion of the fluid into the fibers from the main flow. This is similar to a manifold defined by Bajura and Jones (1976) as a flow channel in which fluid enters or leaves through porous sidewalls due to the action of a differential pressure. All the fluid that comes in through the inlet tube is distributed among the fibers according to the difference of pressures at the two bundle surfaces. In order to obtain the flow distribution among the fibers it becomes necessary to understand clearly the flow with the natures of impinging jet and manifold flow.

Acrivos et al. (1959) studied flow distributions in a dividing-flow manifold using a cylindrical channel to which several smaller conduits are attached at right angles. The pressure rose along the channel due to the deceleration of the fluid. So the fluid velocity at the port near the entrance of the channel was slower than the velocity near the closed end of the manifold. Using the perturbation method and assuming inviscid flow, Scholtz and Trass (1970) calculated the stagnation velocity and the pressure distributions on an impingement surface for a jet flow with a parabolic velocity distribution; they also performed an experiment. The pressure gradient varied with the distance from the stagnation point to the edge of the impingement surface. The maximum pressure occurred at the stagnation point and then decreased with increasing radial distance. If the distance of the jet exit above the impingement surface was short, the local minimum pressure occurred between the center and the edge of the surface. The fluid flow in the forehead of the hollow fiber module possesses the characteristics of the dividing manifold flow and impinging jet. In the backhead of the hollow-fiber module the fluid flow possesses the characteristics of the combining manifold. Because of this the fluid distributions among the fibers are not even, which results in a performance of the device inferior to that with uniform flow distribution. Since the flow suddenly expands from a small inlet tube into a wide manifold, the formation of a recirculating region is anticipated. This can be a serious problem in an artificial kidney, as it forces a portion of the blood to stay longer than necessary. Thus it becomes necessary to examine this problem theoretically as well as experimentally.

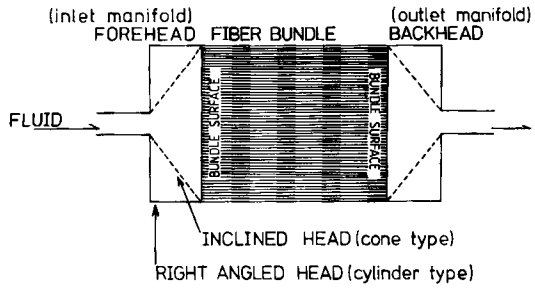

Figure 1. Hollow-fiber module

Most hollow-fiber devices have a manifold whose shape is a cylinder (right-angled), a cone (inclined), or a combination of the two. Since many thousands of the fibers are imbedded in the bundle, we can treat the bundle surface as a porous wall. This assumption makes possible a numerical approach to the problem. The present investigation aims at studying the flow distributions, taking into account the effects of the manifold shape the existence of the downstream manifold, the height of manifold head, the pressure factor in the fibers, and the Reynolds number.

Governing Equations and Computational Scheme

If we assume that the fluid is Newtonian, the fluid velocities in the hollow fibers are determined by the pressure differentials

between the two manifold surfaces. Because the flow in the manifold head is three-dimensional and axisymmetric, we can write dimensionless governing equations for the vorticity, the stream function, and the pressure in cylindrical coordinates as follows:

$$u_r \frac{\partial \omega}{\partial r} + \frac{u_r}{r}\omega + u_z \frac{\partial \omega}{\partial z} = \frac{1}{RE}\left\{\frac{\partial}{\partial r}\left[\frac{1}{r}\frac{\partial}{\partial r}(r\omega)\right] + \frac{\partial^2 \omega}{\partial z^2}\right\} \quad (1)$$

$$\omega = \frac{1}{r}\frac{\partial^2 \psi}{\partial z^2} + \frac{1}{r}\frac{\partial^2 \psi}{\partial r^2} - \frac{1}{r^2}\frac{\partial \psi}{\partial r} \quad (2)$$

$$-\nabla^2 p = -\frac{\partial u_z}{\partial z}\frac{\partial u_r}{\partial r} + u_r \frac{\partial}{\partial r}\left(-\frac{u_r}{r}\right) + 2\frac{\partial u_r}{\partial z}\frac{\partial u_z}{\partial r} + \left(\frac{\partial u_z}{\partial z}\right)^2 \quad (3)$$

From the continuity equation the velocity components are given, respectively, by:

$$u_r = \frac{1}{r}\frac{\partial \psi}{\partial z}, \quad u_z = -\frac{1}{r}\frac{\partial \psi}{\partial r} \quad (4)$$

where the Reynolds number (RE) is based on the bundle diameter Ro and the superficial velocity in the bundle. Table 1 lists the dimensionless variables used in the computation. Dimensionless Eqs. 1 and 2 are derived easily using the dimensionless variables from the dimensional equations given by Currie (1974). The Poisson form of the pressure equation can be derived following the procedure for the rectangular coordinates suggested by Roache (1976). Using the computational scheme shown in Figure 2 we solve the above governing equations by the finite-difference method. The initial values of the stream function, vorticity, and pressure are assumed at all grid points. Then with the boundary conditions given in Figure 3 the computation is continued until the stream function and the vorticity converge. The convergence condition is such that the relative error $E = (|\phi_{ij}^n - \phi_{ij}^{n-1}|)/|\phi_{max}|$ is less than 1.0×10^{-4} at all grid points. The finite-difference forms of the pressure equation are also calculated with the values of the stream function and the vorticity. However, in practice, only the pressures on the upstream and downstream surfaces of the bundle are calculated to analyze the fluid velocities in the fibers of the bundle. These procedures are repeated until the relative error for the stream function $[(|\psi_{ij}^N - \psi_{ij}^{N-1}|)/|\psi_{ij}^N|]$ is less than 5.0×10^{-3}.

Figure 3 summarizes the boundary conditions used in the computation. Upstream of the inlet tube connected to the forehead manifold, Dirichlet boundary conditions are used for the stream function and the vorticity (boundary 1). These seem

Table 1. Dimensionless Variables

$(1 - AR)$	Portion of hollow fiber in the cross section of the fiber bundle
$R1$	ID of fiber/Ro
$R2$	Fiber length/Ro
$R3$	Radius of inlet tube/Ro
$R4$	Head height/Ro
RE	$Ro\,\rho\,Uo/\mu$
K	$32\,R2/(1 - AR)/R1/R1$
p	Pressure, p'/Uo^2
ψ	Stream function, $\psi/Uo\,Ro^2$
ω	Vorticity, $\omega'\,Ro/Uo$

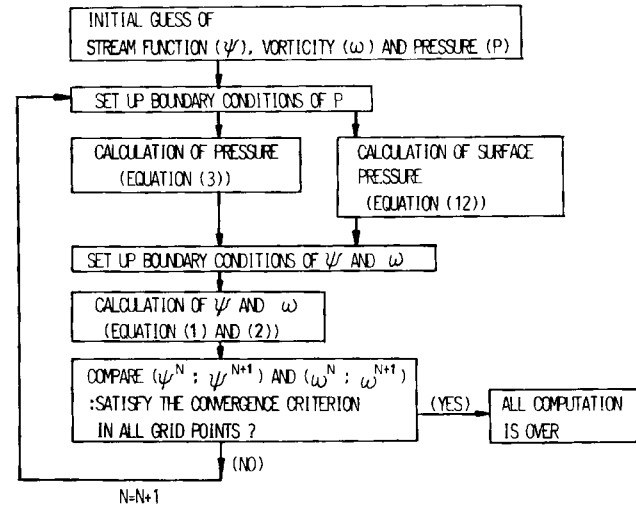

Figure 2. Flow chart of computer algorithm.

appropriate when there is no information available for the fluid velocity in the inlet tube. At the solid wall (boundary 2,3,4,9,10,11) vorticity is of the second-order form for the cylindrical head:

$$\omega = \frac{1}{r}\frac{8\psi_{wall+1} - \psi_{wall+2} - 7\psi_{wall}}{2\,\Delta n^2} \quad (5)$$

For the cone-type manifold we use the first-order form,

$$\omega = \frac{2(\psi_{wall+1} - \psi_{wall})}{r\,\Delta n^2} \quad (6)$$

and for the inclined solid wall (boundary 3,10):

$$\omega_{i,j} = \frac{1}{r_j}\left[\frac{2(\psi_{i+1,j} - \psi_{i,j})^2}{(z_{i+1} - z_i)^2} + \frac{2(\psi_{ij} - \psi_{i,j-1})^2}{(r_j - r_{j-1})^2}\right] \quad (7)$$

The finite-difference equations, Eqs. 5, 6, 7 in the cylindrical coordinates can be derived from those in the rectangular coordinates presented by Roache (1976). The boundary conditions at the surface of the bundle (boundary 6, 7) are very important. Since the diameter of the hollow fiber is about 0.01 of the bundle diameter, we consider that the surface of the bundle is a continuous porous wall and the fluid flow in the nonpermeable fiber is Poiseuille flow. The method of determining the boundary values of the stream function on the surfaces of the bundle is analogous to the technique used for parallel pipe flow (Streeter and Wylie, 1975). The axial fluid velocity is calculated from the pressure

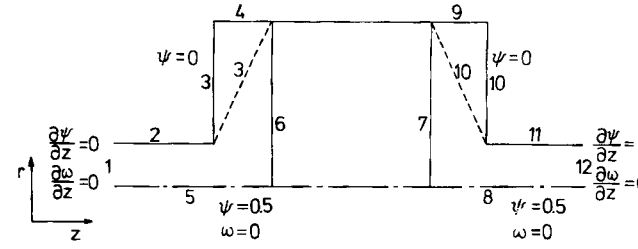

Figure 3. Boundary conditions.

difference between the two surfaces of the bundle according to the following equation:

$$\Delta p_j = \frac{32\,R_2}{RE \cdot R_1^2\,(1 - AR)} \frac{u_j}{} = K \frac{u_j}{RE} \tag{8}$$

Here u_j from Eq. 4 can be written in the finite-difference form for the variable grid space:

$$u_j = -\frac{1}{r_j}\left[\frac{(\psi_{j+1} - \psi_j)(r_j - r_{j-1})}{(r_{j+1} - r_j)(r_{j+1} - r_{j-1})} + \frac{(\psi j - \psi_{j-1})(r_{j+1} - r_j)}{(r_j - r_{j-1})(r_{j+1} - r_{j-1})}\right]$$

For the Poiseuille flow the pressure drop in a single fiber is proportional to the fiber length and inversely proportional to the square of the fiber diameter and $(1 - AR)$ defined in Table 1. So if the pressure factor K is defined as in Table 1, the flow distribution in the fiber bundle can be expressed as a function of K. From Eq. 8 the stream function at the $(j + 1)$th node on the surface of the bundle can be written:

$$\psi_{j+1} = \psi_j - \frac{RE \cdot \Delta p_j r_j (r_{j+1} - r_j)(r_{j+1} - r_{j-1})}{K(r_j - r_{j-1})} - \frac{(\psi_j - \psi_{j-1})(r_{j+1} - r_j)^2}{(r_j - r_{j-1})^2} \tag{9}$$

The stream function at the edge node that was calculated by the successive insertion methods using those of the first and the second nodes does not necessary meet the zero boundary condition at the solid wall. This means that the calculated flow rate through the bundle is not equal to the actual rate. Thus the following corrections are made:

$$\frac{0.5 - 0}{0.5 - \psi_{\text{edge}}} = \frac{0.5 - \psi_{j,\text{corrected value}}}{0.5 - \psi_j} \tag{10}$$

The stream function at the edge node obtained from Eq. 9 converges to zero as the computation in Figure 2 continues. The vorticity on the porous wall (boundary 6, 7) can be presented by

$$\omega = \frac{1}{r}\frac{\partial^2 \psi}{\partial z^2} - \frac{1}{r^2}\frac{\partial \psi}{\partial r} + \frac{1}{r}\frac{\partial^2 \psi}{\partial r^2} \tag{11}$$

The pressure gradient only with axial velocity on the porous wall is given by

$$\frac{\partial p}{\partial r} = -u_z \frac{\partial u_r}{\partial z} + \frac{1}{RE}\frac{\partial \omega}{\partial z} \tag{12}$$

The pressure at the center of the outlet surface of the bundle is calculated from that of the inlet surface:

$$p_{\text{back},1} = p_{\text{fore},1} - \frac{K}{RE} u_1 \tag{13}$$

At the center of the bundle surface the axial velocity from Eq. 4 is indeterminate. Applying L'Hospital's rule to Eq. 4, the axial velocity at the center of the surface is derived as by Hornbeck et al. (1963):

$$u_1 = \frac{2(\psi_1 - \psi_2)}{(r_2 - r_1)^2} \tag{14}$$

The subscripts 1,2 in Eqs. 13 and 14 are the node numbers of the center (first) and the next (second) grid point on the bundle surface (boundary 6 in Figure 3).

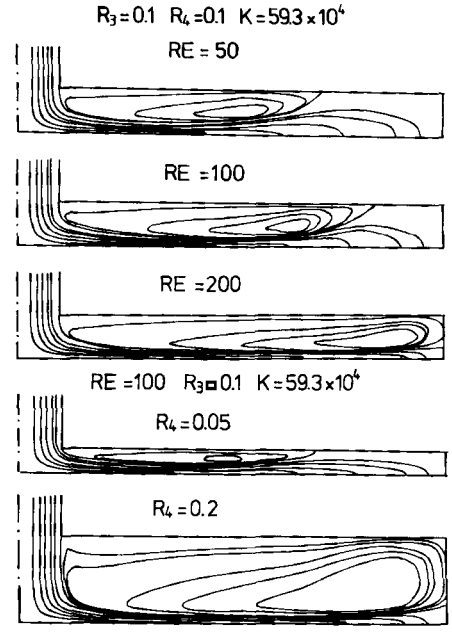

Figure 4. Streamline distributions in an upstream cylindrical manifold.

RESULTS AND DISCUSSION

Numerical method

The vorticity transport equation was discretized according to the first upwind difference form and variable grid space was introduced to the system. Grid lines were concentrated in the region where the fluid motion varied abruptly. Near the wall the ratio did not exceed 1.5 at any region, guided by Gosman et al. (1969). The Gauss-Seidel method was used to solve the stream function equation and the underrelaxation method was used for the vorticity transport equation.

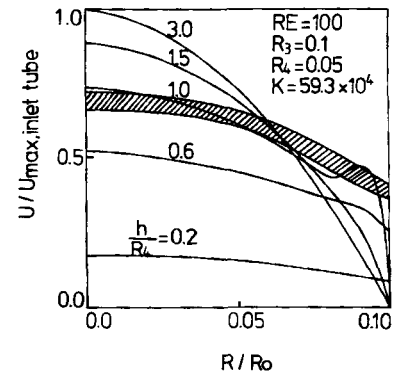

Figure 5. Velocity profiles at the inlet tube into a cylindrical manifold.

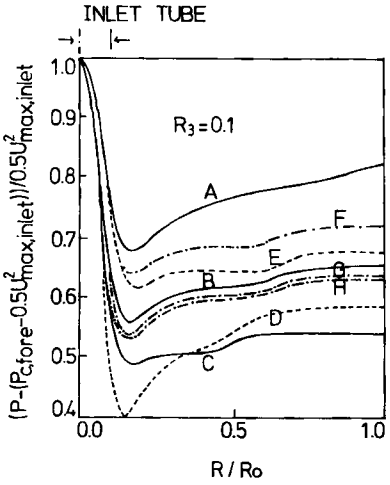

Figure 6. Pressure distributions on the fiber bundle surface.

Fixed manifold height $R4 = 0.1$ $K = 59.3 \times 10^4$
A, B, C, D, E, F, G, H all in cylindrical manifold.
A. $RE = 200$; B. $RE = 100$; C. $RE = 50$.
Fixed $RE = 100$, $K = 59.3 \times 10^4$
D. $R4 = 0.05$; E. $R4 = 0.2$.
Height $R4 = 0.1$, $RE = 100$
F. $K = 21.3 \times 10^4$; G. $K = 133.3 \times 10^4$; H. $K = 533 \times 10^4$.

The Reynolds number encountered in commercial artificial kidney operations is about 50 and that in the reverse osmosis module is about 1,000. In this study we varied the Reynolds number from 50 to 200, above which computation diverged in some cases. The finite-difference equations for the cone-type manifold diverged at a high RE and a small K value. The stream functions on the porous surface (boundary 6, 7 in Figure 3) calculated from the surface pressure of the $N + 1$ step were very different from those of the N step. Thus the underrelaxation concept was introduced as follows:

$$\psi_j^{N+1} = \psi_j^N + 0.1\,(\psi_{j,\text{corrected value}}^{N+1} - \psi_j^N) \qquad (15)$$

The difference in the flow distributions in the module calculated by the first-order and by the second-order forms of the vorticity at any corresponding point was within 1% of the flow.

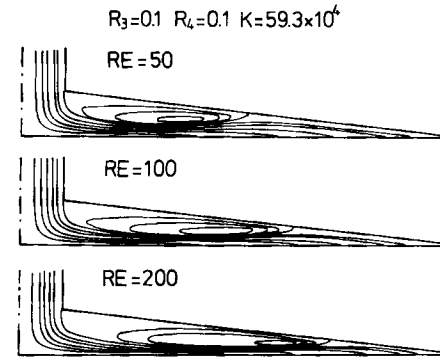

Figure 8. Streamline distributions in a cone-type manifold.

Flow distributions in the hollow-fiber module with one cylindrical manifold

In order to see the effect of the upstream manifold on the flow distribution, numerical study was performed for the module with one cylindrical manifold. The computational scheme for one manifold is the same as that for two manifolds given in Figure 2. The stream function distribution on the inlet surface of the bundle (6 in Figure 3) is the same as that of the outlet bundle surface (7 in Figure 3) because the fluid flows through the fibers in the bundle. But for one manifold, the pressure on the outlet bundle surface is atmospheric at all points, like the experimental system of Agish et al. (1975). For two manifolds, in the step "Calculation of Surface Pressure" in Figure 2, the pressure on the outlet surface of the bundle is calculated with $P_{\text{back},1}$ from Eq. 13 and pressure gradient from Eq. 12. For one manifold, in this step the pressure on the outlet surface is considered as $P_{\text{back},1}$. And the stream function and vorticity in the backhead need not to be calculated in the step "Calculation of ψ and ω" in Figure 2 because backhead does not exist.

Figure 4 shows the streamlines in the upstream manifold with seepage through the bundle surface whose total equals the inlet flow rate. We can see the combined characteristics of impinging jet and dividing manifold flow. Pseudostagnation flow is built up at the center region on the surface of the bundle and an eddy of considerable size is formed between boundaries 3 and 6 of Figure 3. The eddy grows and its center moves toward the edge of

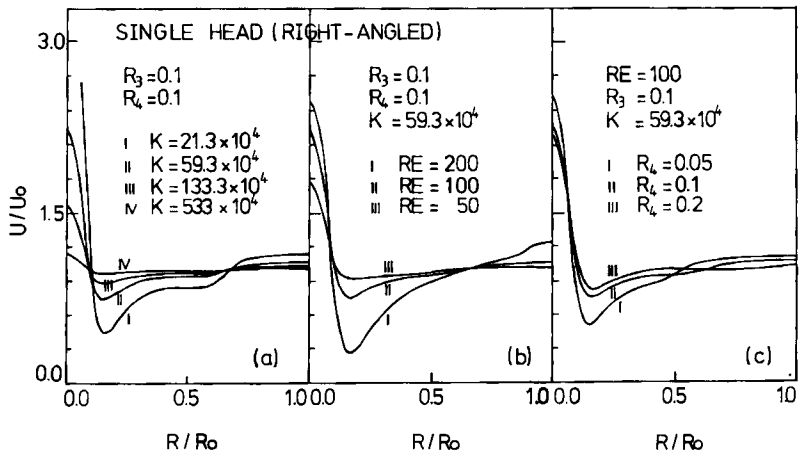

Figure 7. Flow distributions in the fiber bundle with a cylindrical manifold.

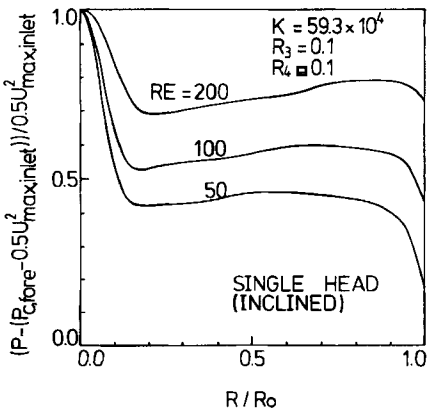

Figure 9. Pressure distributions in a cone-type manifold.

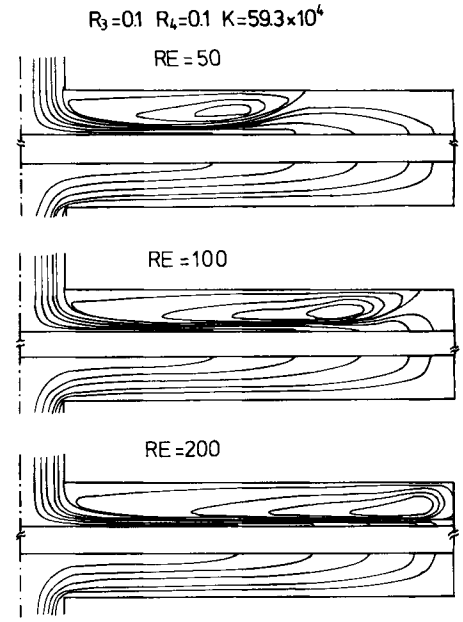

Figure 11. Streamline distributions with two cylindrical manifolds.

the manifold as the Reynolds number increases. The size of the eddy increases with the manifold height. The separation of flow in a diverging channel is quite natural, but the presence of the porous lower wall confines its size between the upper wall and the thin layer of radial flow. As RE increases the eddy center is carried toward the edge by the fast radial flow.

It is easily conceivable that the velocity profile in the inlet tube distant from the manifold is that of Poiseuille flow. Figure 5 shows the approaching velocity profiles at the manifold inlet. If the manifold height is sufficiently large ($R3/R4 < 0.5$), the profile remains Poiseuille-type as it approaches the manifold. As the head height becomes smaller, the profile deviates from that of Poiseuille flow and the flow becomes faster near the edge ($R3/R4 = 2$). As the fluid approaches closer to the bundle surface, the axial component of the velocity is retarded due to the presence of the stagnation wall and becomes constant independent of the radial coordinate. The inlet profile was relatively insensitive to the Reynolds number and the characteristics of the bundle. The shaded portion in Figure 5 represents the experimental results in the wall jet obtained by Sholtz and Trass (1970), which support the present results.

Figure 6 shows the pressure patterns on the surface of the bundle. $U_{max,inlet}$ in the vertical axis of Figure 6 is the dimensionless maximum velocity in the inlet tube and $0.5\ U^2_{max,inlet}$ is the dimensionless stagnation pressure at the center of the inlet surface of the bundle. The pressure on the surface reaches a maximum at the stagnation point and then decreases rapidly due to the buildup of radial velocity. However, the radial velocity decreases because of the continuity equation. Therefore the pressure increases again, which is also evident from Eq. 12. Thus the minimum occurs near the center. In other words, the first term in Eq. 12 contributes to the pressure rise due to the negative radial velocity gradient. Also, between the minimum pressure point and the edge there are regions where the pressure change is larger (A, B, C, D, E, Figure 6). These are the places where the centers of the eddy are located and the flow path under the eddy becomes broad. The rate of pressure change becomes larger with the increase of RE and the decrease of the manifold height. The same is true for the minimum pressure.

The pressure patterns on the surface of the bundle, except in the center region, resemble each other as the bundle characteristic K varies (B, F, G, H, Figure 6) because the streamline pat-

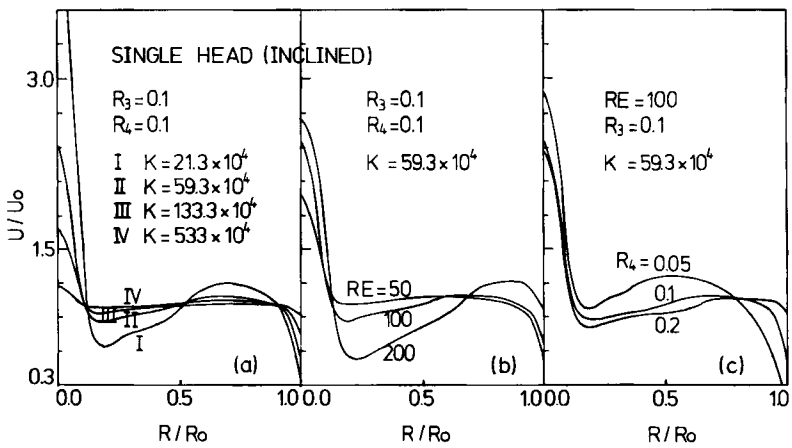

Figure 10. Flow distributions in the fiber bundle with a cone-type manifold.

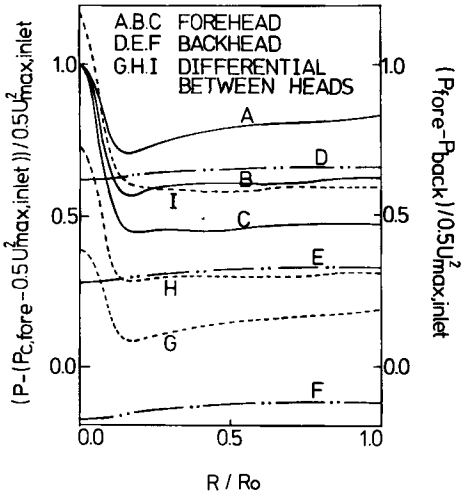

Figure 12. Pressure distributions on the fiber bundle surface.

Fixed head height $R4 = 0.1$, fixed $K = 59.3 \times 10^4$
A, D, G. $RE = 200$, two cylindrical manifolds.
B, E, H. $RE = 100$, two cylindrical manifolds.
C, F, I. $RE = 50$, two cylindrical manifolds.

terns are not varied much with K, which represents the resistance for the fluid flow in the hollow fibers. The pressure at the minimum point becomes larger with increase of K value because the first term on the righthand side of Eq. 12 becomes smaller with increasing K value. The pressure drop in a single fiber is proportional to K and inversely to RE, as shown in Eq. 8. Thus the average velocity in each fiber is determined by K, RE, and the pressure at the inlet and the outlet of the fiber. The velocity difference becomes wider as K becomes smaller and RE larger, Figure 7. If the pressure drop through the fibers is small (smaller K), the flow tends to go through the fibers near the center. For instance, the velocity difference between the edge and the minimum point is 0.02 Uo for $K = 533 \times 10^4$, and 0.60 Uo for $K = 21.3 \times 10^4$. The maximum velocity at the center is 1.1 Uo for $K = 533 \times 10^4$, and 3.7 Uo at $K = 21.3 \times 10^4$. The pressure difference between the minimum point and the edge for $RE = 200$ is 2.5 times that at $RE = 50$ (Figure 6). The velocity differences between the two points are 0.1 Uo at $RE = 50$, and

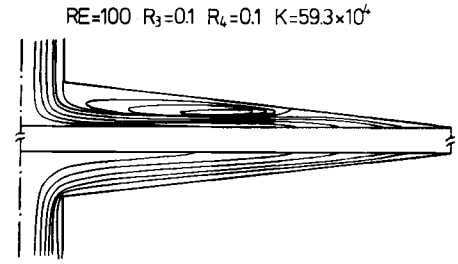

Figure 14. Streamline distributions in the fiber bundle with two cone-type manifolds.

1.0 Uo at $RE = 200$ (Figure 7b). For the different manifold heights the pressure difference between the two points at $R4 = 0.05$ is three times that for $R4 = 0.2$, and the velocity difference is 0.6 Uo for $R4 = 0.05$ and 0.20 Uo for $R4 = 0.20$ (Figure 7c).

Flow distribution in the module with one cone-type manifold

The size of the eddy in the cone-type manifold is smaller than that in the cylindrical manifold, as shown in Figure 8. The fluid passage under the eddy becomes narrower with increasing radial distance. Figure 9 shows that the characteristics are similar to those in the cylindrical manifold. The maximum pressure occurs at the center and the rate of pressure change resembles closely that in the cylindrical manifold. However, because of the narrow flow path the drop in the radial velocity with increasing distance is much less, compared to that in the cylindrical manifold. The radial velocity near the edge is still high, which keeps the pressure in the region relatively low. We have another pressure minimum at the edge of the bundle. This pressure decrease is caused by the viscous forces of the two joining walls. In general, the effects of the manifold height and the bundle characteristics K are less than in the cylindrical manifold.

The fluid velocity in the fiber bundle shows two local maxima and two local minima, which reflects the pressure profile on the surface, Figure 10. The positions of these points were nearly unchanged for different K as long as the manifold height and the Reynolds number were the same. Unlike in the cylindrical manifold, the velocity at the edge fell below the average velocity. At a low K the flow at the edge was nearly zero, which results in an

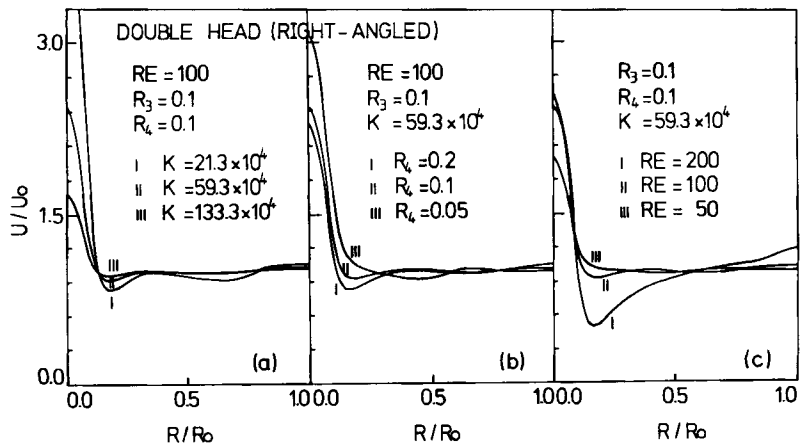

Figure 13. Flow distributions in the fiber bundle with two cylindrical manifolds.

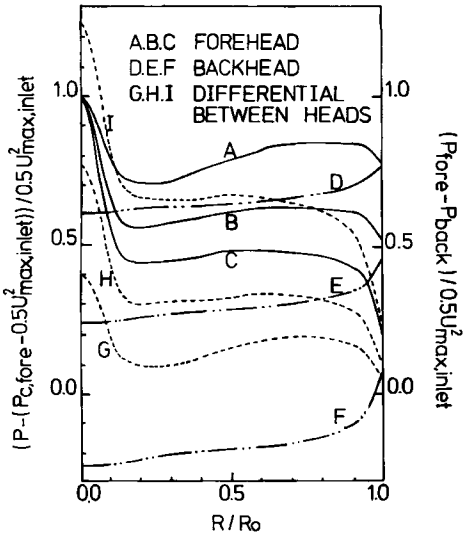

Figure 15. Pressure distributions on the fiber bundle surface.

Fixed head height $R4 = 0.1$, $K = 59.3 \times 10^4$
A, D, G. $RE = 200$
B, E, H. $RE = 100$
C, F, I. $RE = 50$

insufficient use of the fibers in the periphery region where most fibers are located. This is directly connected with the efficiency of the module. The same effects occurs in the case of RE change, Figure 10b. The effect is most serious when the manifold is very low ($R4 = 0.05$). In this case the pressure drop by the viscous forces of the two joining walls nearly blocks the flow at the edge.

Flow distribution in the module with two cylindrical manifolds

The actual flow distribution in the module is determined by the characteristics of the impinging jet and dividing manifold in the upstream manifold and the combining downstream manifold. In the downstream manifold no recirculating flows form, Figure 11. The pressure distributions at the two surfaces of the bundle are shown in Figure 12. The difference of the pressure drop through a fiber between the local minimum point and the edge of the bundle is smaller than that of the module with a single cylindrical manifold. Thus the pressure of the downstream manifold keeps the pressure drop through each fiber in the bundle more uniform, compared to those with one manifold. This happens because the high pressure in the edge region of the upstream manifold is also compensated by the high pressure in the edge of the downstream manifold. Because of this the flow distribution in the center is similar to that of one manifold, but in the rest of the bundle the flow distribution is remarkably uniform with different K's and manifold heights, Figures 13a,b.

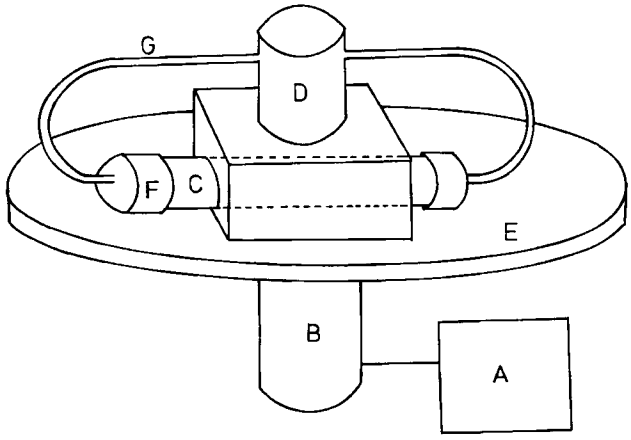

Figure 16. Diagram of potting system.

A. Voltage transformer
B. Motor
C. Fiber bundle
D. Bottle of polyurethane
E. Circular plate
F. Aluminum casing
G. PVA tube

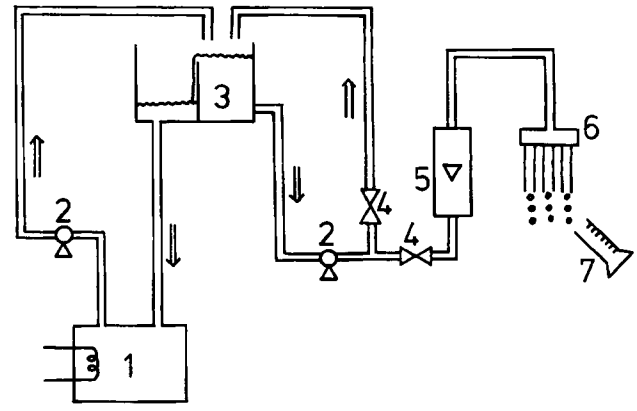

Figure 17. Diagram for measuring flow rate in a hollow fiber.

1. Constant-temperature bath
2. Pump
3. Head tank
4. Valve
5. Flow meter
6. Hollow-fiber reactor
7. Volumetric graduated cylinder

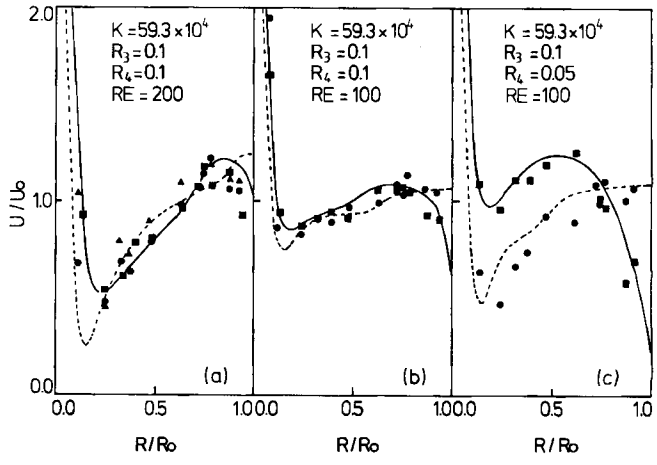

Figure 18. Flow distribution in the hollow-fiber bundle joined with a single head.

In (a) ●▲ represent first and second experiments
●▲ ---- Cylindrical head
■ ____ Conical head

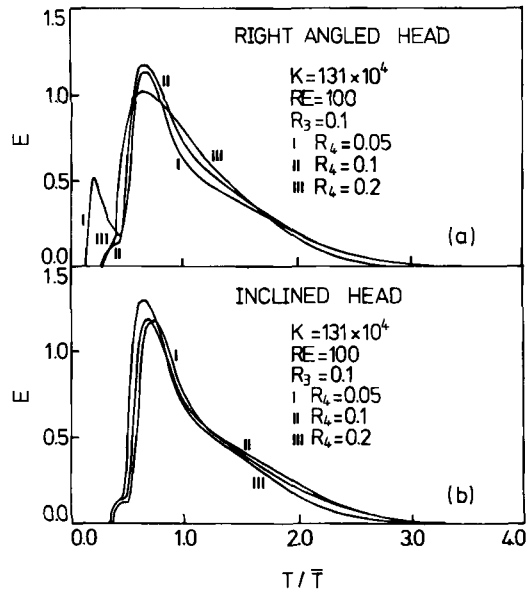

Figure 19. Experimental normalized residence time distribution curve.

But at high Reynolds number we still have a nonuniform profile, Figure 13c.

Flow distribution in the module with two cone-type manifolds

Figure 14 shows the distribution of the stream function in the two cone-type manifolds. The eddy formed in the upstream manifold is nearly the same as that formed in the module with a single cone-type head. The pressure drops through the fibers become more uniform with the attachment of the downstream manifold. But outside of the maximum pressure point the pressure drop through a fiber becomes much smaller than that in the module with a single cone-type head, Figure 15. The pressure differentials in the edge region of the bundle are nearly zero for high Reynolds numbers, small K's, and lower manifold heights (Park, 1985). In other words, there is virtually no fluid flow in the fibers in the edge region of the bundle.

Experimental Verification

Apparatus and procedures

The outer case of the bundle was prepared by machining a transparent Lucite cylinder of 20 cm (effective flow path) length to a pipe of 4 cm ID. As an impermeable hollow fiber we chose propylene tubes of 810 (±24) μm ID. The number of fibers used in making a bundle is 364 in this experiment. The fibers were stuck to tape of 2 cm width and then were rolled up. This helped each fiber to keep its own radial position in both the inlet head and outlet head of the bundle when polymer was injected between the fibers. Some fibers were marked with various colors in order to detect easily the radial position of the fibers on the inlet surface of the bundle. The flow rates of the fluid that passed through these fibers were measured. The bundle of the fibers was inserted into the bundle case and polyurethane was injected. Polyurethane was prepared by mixing isocyanate polymer PUR725A and polyol PUR725B (Wikolin Polymer Company, West Germany). The mixed polymer was immediately transferred to the aluminum cup, D in Figure 16, and fed into the aluminum casing F attached at the ends of the bundle by the centrifugal force created by the rotation of plate E attached to the DC motor, B. By properly adjusting the amount of the polymer in the cup we could control the penetration depth of the polymer between the fibers. The polymer did not penetrate through the fiber because the air trapped in the fiber keeps the polymer from penetrating into the two ends of the fiber. After 30 min of rotation, the cured polyurethane was cut to a desired length with a microtome. The cross section cut by the microtome is the bundle surface. The length of the bundle was 20 cm. The cylindrical or conical heads, prepared as desired, were fitted to the bundle by a thread. The bundle with one manifold was obtained by cutting out one head of the bundle made by the procedure described above. Figure 17 shows a schematic diagram of the experimental system. A head tank with constant temperature was used and the flow rate was controlled by the valve and the flow meter. The flow rate through a marked fiber whose radial position on the surface of the bundle was known was measured by a volumetric graduated cylinder. Duplicate measurements were made to ensure reproducibility.

In order to measure the flow distribution in the bundle with the upstream and downstream manifolds, the residence time distribution method and photographic analysis were used. KCl solution was used as a tracer and injected at the inlet tube as the impulse; detection downstream was carried out continuously with a platinum electrode prepared by the method of Khang and Fitzerald (1975). For rapid photography, a black ink tracer was injected at the inlet tube and the tracer in the downstream manifold was picked up by a high-speed campera (HYCAM, Redlake Corp., U.S.A.) positioned as shown in Figure 20. The camera was capable of taking 10,000 frames per second (fps) continuously; in this experiment we used 160 fps.

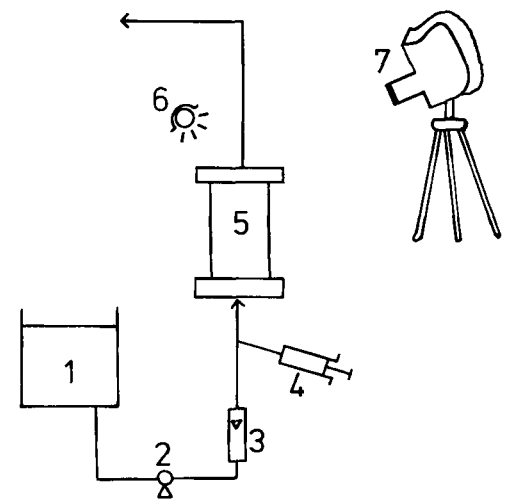

Figure 20. Flow sheet for flow visualization.

1. Reservoir tank
2. Pump
3. Flow meter
4. Dye injector
5. Hollow-fiber reactor
6. Light
7. HYCAM

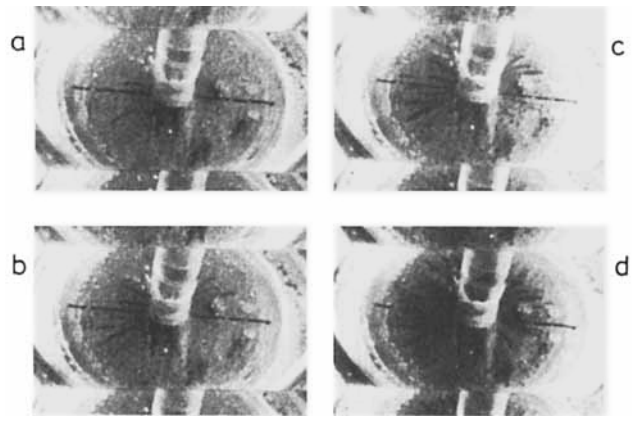

Figure 21. Photographs of the appearance of dye (cone-type heads).

$RE = 200$; $K = 131 \times 10^4$; $R3 = 0.1$; $R4 = 0.1$
(a) $T/To = 0.73$ (c) $T/To = 0.80$
(b) $T/To = 0.79$ (d) $T/To = 0.82$

Flow distribution in the bundle

Figure 18 shows the effects of RE and manifold height on the flow distributions of the bundle with a cylindrical manifold. The experimental results are generally in good agreement with the theoretical predictions denoted by the dotted lines. Figure 18a shows the scattering of the data between the two experiments. When the manifold height is very low ($R4 = 0.05$), the experimental data were a little off the predictions (Figure 18c). Here a question arises whether the assumption of the continuous porous wall hypothesis is still valid. If we consider that the ratio of the height of the manifold to fiber diameter is less than 2, this assumption may not hold. The velocity distributions of the bundle with one conical manifold are also in good agreement with the predictions. Figure 19 shows the residence time distribution in the bundle with the upstream and downstream manifolds. The interpretation of the curve requires the understanding of the flow path and the subsequent modeling. The RTD curve has small and large peak and a long tail. The small peak means that the fluid at the center passes the fiber faster than the rest does.

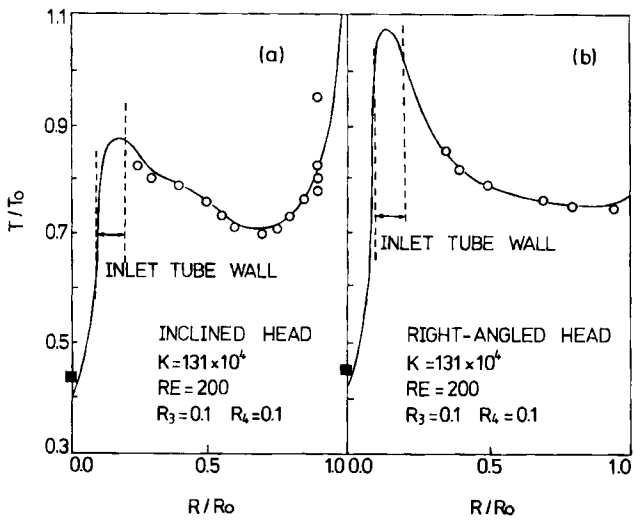

Figure 22. Dimensionless time for dye to pass the hollow-fiber reactor.

The long tail in each figure represents recirculation in the upstream manifold. Figure 19a shows the effect of the height of the cylindrical head on the RTD. The size of the front peak is small if the head height ($R4$) is higher than 0.1. If the head height is very low ($R4 = 0.05$), the front peak becomes large, meaning that the fluid velocity at the center is much faster than the predicted value and the assumption of a continuous porous wall may not hold if the head height is too low. Figure 19b shows the RTD in the reactor with two conical manifolds. Unlike the case with two cylindrical manifolds, the front peak is small even if the head height is very low ($R4 = 0.05$). The small peak which appears ahead of the main RTD curve grows inversely with the head height, which is in good agreement with the higher center velocity predicted numerically. Figure 20 shows the schematic diagram for high-speed photography of the motion of the black ink tracer in the backhead, which has been injected at the inlet tube in the pulse type. Figure 21 shows the motion of the black ink dye photographed at $RE = 200$ in the backhead of the module with two conical manifolds. There is a solid black line across the diameter of the manifold. This was drawn to adjust focus on the bundle surface in photographing. The dye appeared first in the middle region between the center and the edge of the back surface of the bundle. The reference time To was 2 s at $RE = 200$. The residence time predicted numerically is shown by the curve in Figure 22. The experimental results from the photographs denoted by the circles were in good agreement with those numerically predicted. At the center region ($r < 0.1$) the residence time was measured with a stopwatch because photography of the region was not possible.

Acknowledgment

The authors are indebted to the Korea Green Cross Medical Equipment Corporation for partial support of this research and also to G. M. Homsey of Stanford University for suggesting boundary conditions on the bundle surface.

Notation

$(1 - AR)$ = ratio of volume of lumen of fibers to that of the hollow fiber bundle
E = distribution function for residence time
h = axial distance from surface of bundle, h'/Ro
K = pressure drop parameter in fiber
n = normal coordinate, n'/Ro
p = pressure, $p'/\rho Uo^2$
Q = volumetric flow rate, cm^3/s
r = radial coordinate, r'/Ro
Ro = radius of fiber bundle, cm
$R1$ = ratio of inner diameter of fiber to Ro
$R2$ = ratio of fiber length to Ro
$R3$ = ratio of radius of inlet tube to Ro
$R4$ = ratio of head height to Ro
RE = Reynolds number, $Ro \cdot Uo/\nu$
T = time, s
To = reference time represented by Ro/Uo, s
$\bar{T}$ = mean residence time in the hollow fiber reactor, s
u = velocity, subscript denotes direction, u'/Uo
Uo = average velocity in fiber bundle, $Q/\pi Ro^2$, cm/s
z = axial coordinate, z'/Ro

Greek letters

ν = kinematic viscosity, cm^2/s
ρ = density, g/cm^3
ψ = stream function, $\psi'/Uo \cdot Ro^2$
ω = vorticity, $\omega' Ro/Uo$
ϕ = dependent variable, vorticity or stream function
ϕ_{max} = maximum value of ϕ in $(n - 1)$th iteration

Superscripts

n = iteration number in step N
N = step number, Figure 2
$'$ = dimensional quantity of given variable

Subscripts

c = center position
back = outlet surface of bundle
fore = inlet surface of bundle
max = maximum
inlet = inlet tube
i = ith node in z coordinate
j = jth node in r coordinate

Literature cited

Acrivos, A., D. B. Babcock, and R. L. Pigford, "Flow Distribution in Manifolds," *Chem. Eng. Sci.*, **10,** 112 (1959).

Agish, T., K. Ota, and Y. Nose, "Is Hollow-Fiber Occlusion Due to Maldistribution of Blood?" *Proc. Eur. Dial. Transplant Assoc.*, **12,** 519 (1975).

Babcock, W. C., R. W. Baker, D. J. Kelly, and E. D. Lachapelle, "Coupled Transport Membranes for Uranium Recovery," *Membrane Extractions*, I.S.E.C. (1980).

Bajura, R. A., and E. H. Jones, Jr., "Flow Distribution Manifold," *J. Fluid Eng., Trans. ASME*, **98,** 654 (1976).

Currie, I. G., *Fundamental Mechanics of Fluids*, McGraw-Hill, New York (1974).

Engasser, J. M., J. Cauman, and A. Mare, "Hollow-Fiber Enzyme Reactors for Maltose and Starch Hydrolysis," *Chem. Eng. Sci.*, **35,** 99 (1980).

Gosman, A. D., W. M. Pun, A. K. Runchal, D. B. Spalding, and M. Wolfstein, *Heat and Mass Transfer in Recirculating Flows*, Academic Press, London (1969).

Hornbeck, R. W., W. T. Rouleau, and F. Osterle, "Laminar Entry Problem in Porous Tubes," *Phys. Fluids*, **6,** 1649 (1963).

Inloes, D. S., W. J. Smith, D. P. Taylor, S. N. Cohen, A. S. Michaels, and C. R. Robertson, "Hollow-Fiber Membrane Bioreactors Using Immobilized *E. coli* for Protein Synthesis," *Biotech. Bioeng.*, **25,** 2653 (1983).

Khang, S. J., and T. J. Fitzgerald, "A New Probe and Circuit for Measuring Electrolyte Conductivity," *Ind. Eng. Chem. Fund.*, **14,** 208 (1975).

Park, J. K., "The Flow Distribution in the Hollow-Fiber Reactor," Ph.D. Diss., KAIST, Seoul, Korea (1985).

Roache, P. J., *Computational Fluid Dynamics*, Hermosa, Albuquerque, NM (1976).

Rony, P. R., "Multiphase Catalysis. II: Hollow-Fiber Catalysis," *Biotech. Bioeng.*, **13,** 431 (1971).

Sholtz, T. M., and O. Trass, "Mass Transfer in a Nonuniform Impinging Jet," *AIChE J.*, **16,** 82 (1970).

Streeter, V. L., and E. B. Wylie, *Fluid Mechanics*, McGraw-Hill, New York (1975).

Manuscript received May 10, 1985, and revision received Feb. 19, 1986.